Journal of Materials Chemistry

Journal of Materials Chemistry A

Dynamic Article Links ►

Cite this: DOI: 10.1039/c0xx00000x

www.rsc.org/xxxxxx

ARTICLE TYPE

Corrosion of molybdate intercalated hydrotalcite coating on AZ31 Mg alloy

Rong-Chang Zeng *[a,b], Zhen-Guo Liu[a], Fen Zhang*[a] , Shuo-Qi Li[a], Hong-Zhi Cui[a] and En-Hou Han[b]

[a] *College of Materials Science and Engineering, Shandong University of Science and Technology, Qingdao 266510, China. E-mail address: rczeng@gmail.com (R.C. Zeng), zhangfen2011@hotmail.com (F. Zhang)*
[b] *Institute of Metals Research, Chinese Academy of Sciences, Shenyang 110016, China.*

Abstract: A molybdate intercalated hydrotalcite (HT-MoO_4^{2-}) coating with nano-sized lamellar structure was synthesized on AZ31 Mg alloy by the combination of the co-precipitation and the hydrothermal process. The characteristics of the coatings were investigated by SEM, EPMA, XRD, EDS and FT-IR. The corrosion resistance of the coatings was assessed by potentiodynamic polarization, electrochemical impedance spectrum and hydrogen evolution. The results indicated that the HT-MoO_4^{2-} coating, characterized by interlocking plate-like nanostructures, ion-exchange and self-healing ability, has a potential to be the "smart" coating capable of response to the stimuli from environment.

1. Introduction

Magnesium alloys have been applied in automobile, aerospace and electronic industry. Unfortunately, they are susceptible to the attack by chlorine ions in an aggressive environment due to their lower potentials. Their applications on a larger scale are thus restricted[1-3]. Therefore, an improvement in corrosion resistance is of critical importance for magnesium alloys. Protective coating systems are normally applied on magnesium surfaces to provide a dense barrier against the corrosive species in order to protect the metal from the attack[4]. A number of surface treatments such as chemical conversion coatings[5-8], micro arc oxidation (MAO) coatings[9], polymer coatings[10], electrochemical plating coatings[11], physical vapor deposition (PVD) coatings[12] and plasma-assisted chemical vapor deposition (PACVD) coatings[13] have been adopted to enhance the corrosion resistance. However, the barrier system can not stop the corrosion process when the coatings are damaged and the corrosive agents penetrate to the magnesium surface. The development of self-healing coatings based on nanostructures has been a route to obtain the so-called "smart" coatings capable of response to the stimuli from environment[14, 15].

It is well-known that layered double hydroxides (LDHs) possess special layered structures. LDHs can be expressed by the general formula: $[M^{2+}_{1-x}M^{3+}_{x}(OH)_2]^{x+}A^{n-}_{x/2}\cdot mH_2O$, where the cations: M^{2+} and M^{3+} reside in the octahedral holes in a brucite-like layer and the anion A^{n-} is positioned in the hydrated interlayer galleries[16]. LDHs have potential applications in flame retardants, heterogeneous catalysts, polymer stabilizers acid absorbents, and biomedical materials[17-19]. One application for LDHs is used as a potential replacement for chromium conversion coating[20, 21] due to their unique structures with potent adsorption, ion-exchange capacity and high corrosion resistance. Also, the LDHs with layered structures as nano-containers may be the best carriers of inhibitors. Recently, substantial LDHs coatings on magnesium alloys have been developed[22]. The in-situ prepared Mg-Al and Mg-Fe hydrotalcite conversion coatings on AZ91 magnesium alloys and pure magnesium formed by Uan[23-28], exhibit high hydrophobicity and corrosion resistance. Also, Chen[29-32] adopted the in situ method to prepare Mg-Al hydrotalcite on AZ31 alloy and then modified the hydrotalcite coating with phytic acid. It is demonstrated that the LDH coatings lead to an enhancement in corrosion resistance of magnesium and its alloys. However, there are still some drawbacks for the in-situ preparation of the Mg-Al-LDH coatings. The complicated synthesis conditions greatly limit the chemical compositions of the main layers and the anions species in the interlayer of the LDHs.

The other application of LDHs coatings were prepared by two steps. Zhang[33-36] investigated the corrosion property of the molybdate pillared hydrotalcites and tungstate pillared hydrotalcites as the pigments in organic coatings on AZ31 alloy. It was found that the interlayer molybdate and tungstate anions of hydrotalcite were partially exchanged with chloride anions by ionic exchange and the invasive chloride ions were held by the hydrotalcite interlayer. The released molybdate and tungstate anions acted as the anodic inhibitor to protect Mg alloys from corrosion due to its passivating ability, which is similar to that of chromates[37]. Fuente[38] synthesized Zn-Al-vanadate hydrotalcite coating on an aluminium alloy by two steps using the co-precipitation method and air-spraying process. Those coatings by the two steps greatly improved the corrosion resistance of their substrates, but the adhesion of the coating to the substrate is much poorer. Thus, the preparation of LDHs coatings on Mg alloys with high corrosion resistance and adhesion to the substrate by a simple technological process remains a considerable challenge. Co-precipitation[39] (CPT) is the carrying down by a precipitate of substances normally soluble under the conditions employed. The CPT is a widely applicable method for preparing LDHs which can precisely control the chemical compositions and has a high reacting activity. CPT and hydrothermal process can together synthesize different systems of LDHs coatings easily, regardless of the substrates, the chemical compositions of the main layers and the anions species in the interlayer.

This paper aims to prepare an nano-sized $Mg_6Al_2(OH)_{16}MoO_4 \cdot 4H_2O$ coating with ion-exchange and self-healing ability by the CPT and hydrothermal treatment on AZ31 Mg alloy, and to take further insight into the corrosion mechanism of the LDH coating.

2. Experimental

2.1 Fabrication of the HT-MoO_4^{2-} coating

Fig. 1

Fig. 1 Experimental process diagram for the fabrication of the HT-MoO_4^{2-} coating

The material used was commercial cast Mg alloy AZ31 with nominal compositions of 3.0 wt % Al, 1.0 wt % Zn and balanced Mg. The ingot was cut into a size of 20 mm × 20 mm × 4.0 mm. The samples was firstly ground to 2000 grit SiC paper, and then ultrasonically cleaned in ethyl alcohol for 15 min, and finally dried by warm air. Molybdate intercalated hydrotalcite (HT-MoO_4^{2-}) coating was prepared by the combination of the CPT and the hydrothermal process (Fig. 1) on the AZ31 Mg alloy. In a typical synthesis, $Mg(NO_3)_2 \cdot 6H_2O$ and $Al(NO_3)_3 \cdot 9H_2O$ with Mg^{2+}/Al^{3+} molar ratio of 2 were dissolved in boiling (to remove CO_2) de-ionized water such that solution A was produced. The mixture of $Na_2MoO_4 \cdot 2H_2O$ with MoO_4^{2-}/Al^{3+} molar ratio of 2 and NaOH with $OH^-/(Mg^{2+}+Al^{3+})$ molar ratio of 2.3 were dissolved in boiling de-ionized water to form the solution B. Solution B was added dropwise to Solution A. The mixture of solutions A and B were maintained at a temperature of 353K for 48 h with vigorous stirring at a pH value of 10.0 under N_2 atmosphere and then aged for 12 h at the same temperature. Finally, the above resultant slurry was transferred to a Teflon-lined autoclave in which the pretreated Mg alloy was immersed. The Teflon-lined autoclave was then heated in a warm chamber at a temperature of 398 K for 36 h. The resultant coating was rinsed with de-ionized water and dried by warm air.

2.2 Surface analysis

The surface morphologies and cross sections of the HT-MoO_4^{2-} coating were discerned via a field-emission scanning electronic microscope (FE-SEM, Hitachi S-4800). All samples for the SEM observation were sputtered with gold. The HT-MoO_4^{2-} coatings as well as the HT-MoO_4^{2-} powder were examined on a X-ray diffraction diffractometer (XRD, D/Max 2500PC) with Cu target (λ= 0.154 nm) at a scanning rate of 0.02 s^{-1} in the 2θ range from 5° to 80°. The HT-MoO_4^{2-} coatings was also probed using Fourier Transform infrared Spectroscopy (FT-IR, TENSOR-27) in the wavenumber range from 500 cm^{-1} to 4000 cm^{-1} at room temperature. The chemical compositions of the coating was inspected through energy-dispersive X-ray spectroscopy (EDS, Oxford Isis), which is affiliated to an electron probe X-ray microanalysis (EPMA).

2.3 Electrochemical test

The potentiodynamic polarization curves and electrochemical impedance spectroscopy (EIS) were performed on an electrochemical workstation (PARSTAT, 2273) in a cell with 3.5 wt. % NaCl solution at room temperature. All the electrochemical tests were conducted in a classical three-electrode system which consists of the sample as the working electrode (1 cm^2), a platinum plate as the counter electrode and a saturated calomel electrode (SCE) as the reference electrode. The polarization curves were recorded at a sweep rate of 2 mV/s. EIS measurements were acquired from 10^5 Hz to 10^{-2} Hz using a 5 mV amplitude perturbation.

3. Results

3.1 SEM morphologies

Fig. 2

Fig. 2 (a, b) SEM micrographs and (c, d) cross-sectional view of the HT-MoO_4^{2-} coating

The SEM morphologies of the prepared HT-MoO_4^{2-} coatings were shown in Fig. 2. It is evident that the HT-MoO_4^{2-} coating (Fig. 2a) is compact over the whole AZ31 Mg alloy substrate. The HT-MoO_4^{2-} coating (Fig. 2b) possesses a compact, homogeneous and well-crystallized nanostructure, which consists of vertically cross-linked nano-plates grown on the substrate. The cross-sectional view (Fig. 2c) of the HT-MoO_4^{2-} coating demonstrates that the coating is fairly compact and thick, and has good adhesion to the Mg alloys. The coating thickness is approximately 17.0 μm. Fig. 2d designates that the sample is composed of non-uniform hexagonal crystals with a size of 300–400 nm. The film shows two structural layers: the dense inner thick-layer and the porous outer thin-layer (Fig. 2d). The results demonstrate that this dense and uniform HT-MoO_4^{2-} coating can avoid the exposure of the substrate to the environment by blocking the penetration of aggressive ions effectively and thus has a potential to act as an environment-friendly and corrosion-resistant film on Mg alloys.

3.2 XRD results

Fig. 3

Fig. 3 XRD patterns of the substrate, HT-MoO_4^{2-} powder and coating

The XRD patterns of the substrate, HT-MoO_4^{2-} ($Mg_6Al_2(OH)_{16}MoO_4 \cdot 4H_2O$) powders and coatings on AZ31 Mg alloy are shown in Fig. 3. The HT-MoO_4^{2-} powder prepared by CPT method displays a typical layered structure characteristic of LDHs with obvious peaks corresponding to the diffraction of the planes: (003) and (006). The interplanar spacings of $d_{(003)}$ and $d_{(006)}$ for the $Mg_6Al_2(OH)_{16}MoO_4 \cdot 4H_2O$ are 7.92 Å and 3.87 Å, respectively. The results are in good agreement with the values of the interplanar spacings reported for the natural hydrotalcite with molybdate in the interlayer[40]. The XRD patterns of Mg alloy with HT-MoO_4^{2-} coatings displayed obvious peaks of LDHs phases at the same angle as the HT-MoO_4^{2-} powder. The results illustrate that the HT-MoO_4^{2-} coatings were successfully deposited on the AZ31 Mg alloy substrate using the hydrothermal process.

3.3 FT-IR spectra

Fig. 4

Fig. 4 FT-IR spectra of the powder and coating

The FT-IR spectra (Fig. 4) of the HT-MoO_4^{2-} powder prepared by the CPT method and the HT-MoO_4^{2-} coating after the hydrothermal process designates the characteristic bands of the LDHs[41-45]. The absorption band at 3696 cm^{-1} corresponds to Mg-O-H stretching vibration due to the magnesia octahedron structure of HT-MoO_4^{2-}, the absorption band at around 3409 cm^{-1} corresponds to O-H because of the presence of the surface absorption water and interlayer water. The shoulder band at around 2931 cm^{-1} corresponds to MoO_4^{2-}-H_2O stretching vibration[35, 36], suggesting the presence of the water-molecule hydrogen bonded to the molybdate ions present in the interlayers. The band at about 1633 cm^{-1} can be ascribed to the bending vibration of crystal water. The band at 1394 cm^{-1} and 621 cm^{-1} can be related with the asymmetric stretching vibration of C-O in CO_3^{2-} ions. The absorption band of CO_3^{2-} ions in the FT-IR spectrum of HT-MoO_4^{2-} may be contaminated by atmospheric CO_2. The characteristic band assigned to the antisymmetric stretching vibration of Mo-O-Mo[35, 36] in MoO_4^{2-} is found at 828 cm^{-1}. Additionally, the bands at 486 cm^{-1} can be attributed to the vibrations mode of the magnesia octahedron at the layer crystal lattice. Therefore, based on the FT-IR spectrum of the HT-MoO_4^{2-}, it can further be confirmed that the HT-MoO_4^{2-} coating has been successfully synthesized on the Mg alloy surface.

3.4 Hydrogen evolution

Fig. 5

Fig. 5 HER of the substrate and HT-MoO_4^{2-} coated sample in 3.5 wt. % NaCl solution

The curves of hydrogen evolution rate (HER) vs. immersion time for the LDH coatings and their substrates are shown in Fig. 5. At the initial stage of the immersion, bubbles emerged on the surface of the AZ31 substrates, while no bubbles were observed on the surface of the HT-MoO_4^{2-} coated samples. Until 48 h after the immersion, little hydrogen gas was produced on the surface of the HT-MoO_4^{2-} coated sample. The HER of the substrates sharply increased during the first two hours and remained at a higher level. The results show that the HER of the coated samples was always controlled at a low level, and can be ignored. After 144 h of immersion, the average HER for the HT-MoO_4^{2-} coated samples was 2.2 $\times10^{-3}$ ml/(cm^2·h) and while for the AZ31 substrates was 4.2 $\times10^{-2}$ ml/(cm^2·h). The result indicates that the HER of the uncoated AZ31 sample is much higher than that of the HT-MoO_4^{2-} coated sample.

3.5 Electrochemical test

Fig. 6

Fig. 6 Tafel polarization curves of the substrate and HT-MoO_4^{2-} coated sample in 3.5 wt. % NaCl solution

Electrochemical test is a commonly used technique that was employed to investigate the corrosion resistance of the conversion coating. Fig. 6 shows the potentiodynamic polarization curves of the prepared hydrotalcite coating after immersion in 3.5 wt % NaCl aqueous solution. As shown in Fig. 6, the corrosion potential (E_{corr}) of the substrate is -1.56 V vs. SCE, while that of the HT-MoO_4^{2-} coated samples is -1.21 V vs. SCE. Based on the polarization measurements, the corrosion current density (I_{corr}) of the substrate is 3.17×10^{-5} A/cm^2, while that of the HT-MoO_4^{2-} coated sample is 1.60×10^{-7} A/cm^2. It is obviously seen that the I_{corr} value of the HT-MoO_4^{2-} coated samples decreased by more than two orders of magnitude compared to the Mg alloy substrate. In addition, there are four breakdown potentials (E_b) and three obvious passivation zones in the anodic branch of polarization curve of the HT-MoO_4^{2-} coated Mg alloy. The reasonable explanation for this result is that the HT-MoO_4^{2-} coatings have a self-healing ability due to the inhibitor activity of the molybdate ions. The results also indicate that the corrosion resistance of AZ31 alloy is effectively enhanced by the HT-MoO_4^{2-} coatings.

Fig. 7a

Fig. 7a Bode plots of the substrate and HT-MoO_4^{2-} coated sample

Fig. 7b

Fig. 7b Nyquist plots of the substrate and HT-MoO_4^{2-} coated sample

Fig. 7c

Fig. 7c The equivalent circuit of the coating

In order to further provide the characteristics of the corrosion inhibition effect of HT-MoO_4^{2-} coating, the EIS was carried out to analyze the corrosion resistance of the coatings. Fig. 7a shows a typical Bode diagram, while Fig. 7b shows a typical Nyquist plot. It is generally known that a higher Z modulus (Fig. 7a) at the lower frequency represents a better corrosion resistance on the metal substrates[46, 47]. It can be seen from the Bode diagram that the HT-MoO_4^{2-} coated sample shows the bigger impedance at the low frequency. Concurrently, it can be observed from the Nyquist plot (Fig. 7b) that the largest radius of the curvature for the HT-MoO_4^{2-} coated sample demonstrates that this sample possesses the highest corrosion protection property. Also, at the lower frequency of the Bode and Nyquist diagram, the trend of the curves indicates a diffusion process, which was attributed to the ion-exchange reaction. The HT-MoO_4^{2-} coating with better EIS performance can effectively prevent the diffusion/penetration of the Cl^- ions to the Mg alloy substrate and thus reduce the corrosion rate of the Mg alloy substrate.

Table 1 Fitting results of EIS spectrum for the HT-MoO_4^{2-} coating

R_S $\Omega\cdot cm^2$	C_{fp} $nF\cdot cm^{-2}$	R_{fp} $\Omega\cdot cm^2$	Y_0 $\mu\Omega^{-1}\cdot cm^{-2}\cdot s^{-1}$	n	R_{fd} $\Omega\cdot cm^2$	C_{del} $nF\cdot cm^{-2}$	R_{ct} $\Omega\cdot cm^2$	Z_w $\mu\Omega^{-0.5}\cdot cm^{-2}\cdot s^{-1}$
7.458	8.058	44.85	1.575	0.591	9273	0.580	11010	122

Journal of Materials Chemistry

Dynamic Article Links ►

Cite this: DOI: 10.1039/c0xx00000x

www.rsc.org/xxxxxx

ARTICLE TYPE

The EIS spectra were analyzed based on the equivalent circuits as shown in Fig. 7c. The data fitting results were listed in Table 1. R_s represents the solution resistance. R_{fp}, which represents the resistance of the outer layer of the HT-MoO_4^{2-} coating, is only 44.85 Ω•cm^2, indicating that the outer layer of the HT-MoO_4^{2-} coating possesses a porous structure (Fig. 1d). C_{fp} represents the capacitance of the outer layer of the HT-MoO_4^{2-} coating at the interface. R_{fd}, which represents the resistance of the inner layer of the HT-MoO_4^{2-} coating, is 9273 Ω•cm^2, showing that the inner layer possesses a dense structure. Constant phase element (CPE) is used in a model in place of a capacitor to compensate for non-homogeneity in the system, which is defined by two values, Y_0 and n ($0 < n < 1$). CPE_{fd} represents the capacitance of the inner layer of the HT-MoO_4^{2-} coating. R_{ct} represents the charge transfer resistance and C_{del} is the electric double layer capacity at the interface. Generally, the larger the value of R_{ct}, the better the coating performs. Hence, the fitting results indicate that the HT-MoO_4^{2-} coated samples exhibit excellent corrosion resistance. Z_w represents the diffusion resistance of the HT-MoO_4^{2-} coating, demonstrating that the HT-MoO_4^{2-} coatings possess the ability for ion-exchange.

4. Discussion

4.1 Corrosion resistance of HT-MoO_4^{2-} coating in comparison to in situ CO_3^{2-}- LDH film

Table 2 Comparison of corrosion rates with different treatment processes

Samples	NaCl wt.%	E_{corr} V/SCE	I_{corr} μA/cm^2	E_b V/SCE	Ref.
AZ31 Substrate	3.5	-1.54	31.72	-1.38	—
HT-MoO_4^{2-} coating	3.5	-1.21	0.16	-0.75	—
In situ LDH film	0.6	-1.47	4.53	-1.28	30
In situ LDH film*	0.6	-1.54	0.76	-1.44	32

* modified by phytic acid

The corrosion resistance of the coatings was assessed by potentiodynamic polarization test. The E_{corr}, I_{corr} and E_b of LDHs with different treatment processes are shown in Table 2. Even in highly concentrated NaCl solution, the corrosion resistance of HT-MoO_4^{2-} coating by far exceeded that of the LDH conversion film prepared by in situ synthesis. Also, there are four E_b and three obvious passivation zones in the anodic polarization curve of the HT-MoO_4^{2-} coated Mg alloy, while the Mg alloy, coated with in situ grown LDH, just has one lower E_b. The results demonstrated that the HT-MoO_4^{2-} coating has corrosion resistance and self-healing ability superior to the in situ CO_3^{2-}-LDH coating.

4.2 Characteristics after immersion

Fig. 8

Fig. 8 Macrographs of (a, b, c) HT-MoO_4^{2-} the coated samples and (d, e, f) the substrates after the hydrogen evolution test

Fig. 8a, b, c and d, e, f show the macrographs of the coated samples and substrates after the hydrogen evolution test in 3.5 wt. % NaCl solutions, respectively. After 144 h of immersion, the most areas of the coated samples (Fig. 8a, b, c) were not attacked except for the localized narrow areas at the edges of the sample, and few corrosion pits were visible on the samples with HT-MoO_4^{2-} coatings. In contrast, serious general corrosion occurred on the substrate (Fig. 8d, e, f). The above results demonstrated that the corrosion resistance performance on the AZ31 Mg alloy was effectively improved by the HT-MoO_4^{2-} coating.

Fig. 9

Fig. 9 SEM micrographs and the corresponding EDS spectra of (a) original HT-MoO_4^{2-} coated sample, (b) sample after corrosion and (c, d,) detailed morphologies of sample after corrosion

Fig. 9 shows the SEM morphologies and their corresponding EDS spectra of the original HT-MoO_4^{2-} coated sample and the immersed sample. The chemical compositions of the original HT-MoO_4^{2-} coated sample (Fig. 9a) was analyzed by spot scanning. It can be seen that the as prepared HT-MoO_4^{2-} coating is mainly composed of Mg, Al, O and Mo elements. The EDS spectrum of the exposed HT-MoO_4^{2-} coating (Fig. 9b) shows Cl and Na peaks after the hydrogen evolution test in 3.5 wt. % NaCl solutions for 144 h. The following results reveal that hydrotalcite present the ion-exchange ability by absorbing Cl^- and Na^+ from NaCl solutions and the EDS results also display that the interlayer of hydrotalcite can be able to retain Cl^- and Na^+ in the hydrotalcite structure. The detailed SEM morphologies of the immersed HT-MoO_4^{2-} coated sample are shown in Fig. 9(c) and (d). It is clear that the HT-MoO_4^{2-} coating on the substrate remained compact and intact with platelet-like microstructure. Also, it can be seen in Fig. 9(c) that some $Mg(OH)_2$ precipitates were covered on the partial surface of the coating, which was ascribed to the dissolution of the Mg substrate and the HT-MoO_4^{2-} coating.

Fig. 10

Fig. 10 The self-healing process of the HT-MoO_4^{2-} coating demonstrated on the cross-sectional views

The self-healing process of the HT-MoO_4^{2-} coating in the corrosive medium is demonstrated on the cross-sectional views of the coatings (Fig. 10). Fig. 10a and b show the cross-sectional views of the coatings before and after 144 h of immersion, respectively. Fig 10c and d designate the magnified morphologies and their corresponding EDS spectra of the original and the immersed coating, respectively. It was revealed in Fig. 10b that the coating contained two layers: the newly formed outer layer and the thinned inner HT-MoO_4^{2-} coating after 144 h of immersion in NaCl solutions. It is also found that the coating morphology has been changed. The non-uniform hexagonal flakes of the HT-MoO_4^{2-} coating (Fig. 10c) were changed into round and bar-like particles (Fig. 10d). The EDS spectrum in the inset of Fig. 10d indicates that the main components of the outer coating is $Mg(OH)_2$. A reasonable explanation for this is that the diffusion of Mg^{2+} ions and OH^- ions, coming from the dissolved Mg substrate and the HT-MoO_4^{2-} coating into the solution leads to the formation of the protective $Mg(OH)_2$ layer. The cross-sectional views results agreed well with the top SEM morphologies. And the $Mg(OH)_2$ layer has a good adhesion to the HT-MoO_4^{2-} coating. It is noting that the total thickness of the protective $Mg(OH)_2$ layer and the HT-MoO_4^{2-} coating was almost not reduced. The results indicate that the HT-MoO_4^{2-} coating do have a self-healing ability.

Fig. 11a

Fig. 11a XRD patterns of the original HT-MoO_4^{2-} coated sample and immersed sample with different time

Fig. 11b

Fig. 11b Detail XRD patterns of (003)

The XRD patterns of the original HT-MoO_4^{2-} coated sample and the samples after different immersion times are shown in Fig. 11a. Coincide exactly with the cross-sectional views results (Fig. 10), Obvious $Mg(OH)_2$ peaks appeared on the immersed samples in addition to those of the HT-MoO_4^{2-} layer and the Mg substrate. With the extension immersion time, it can be seen from Fig. 11 that the intensity of $Mg(OH)_2$ peaks increased, while the intensity of HT-MoO_4^{2-} peaks decreased, the peak at 22.5° nearly disappeared after the immersion of 12 days. But, it can be seen that the peaks of the HT-MoO_4^{2-} coating on AZ31 Mg substrate still existed after 12 days immersion test, which indicated that the HT-MoO_4^{2-} coating had a good corrosion resistance. The peaks position of (003) were shifted to large angle of approximate 0.2° (Fig.11b), indicating that the chloride ions were intercalated by ion-exchange.

Fig. 12

Fig. 12 FT-IR spectra of the HT-MoO_4^{2-} coating before and after the immersion with different time

Further investigations on FT-IR also demonstrated the results analogous to that obtained from the XRD and EDS analysis. The characteristic band (Fig. 12) at the peak of 828 cm^{-1} assigned to the antisymmetric stretching vibration of Mo-O-Mo in MoO_4^{2-} ions had gradually weakened with the prolonging immersion time. The results indicated that the HT-MoO_4^{2-} coating had the ion-exchange ability and released MoO_4^{2-} ions into the corrosive medium. Meanwhile, the other characteristic band of HT-MoO_4^{2-} remain unchanged, which demonstrated that the HT-MoO_4^{2-} coating had a very stability structure.

4.3 Corrosion mechanism.

As is well-known, chlorides, even in small amounts, typically damage the $Mg(OH)_2$ film on the Mg alloy surface continuously because of the replacement of OH^- ions with Cl^- ions and the high solubility of $MgCl_2$ in water[48, 49]. The dissolution reaction of the $Mg(OH)_2$ film on the Mg alloy surface in chloride solution can be given as follows:

$$Mg(OH)_2 + Cl^- \rightarrow Mg(OH)Cl + OH^- \quad (1)$$

$$Mg(OH)Cl + Cl^- \rightarrow MgCl_2 + OH^- \quad (2)$$

In contrast with the common $Mg(OH)_2$ coating, the developed HT-MoO_4^{2-} coating had a much greater corrosion resistance because of the exhibition of the ion-exchange capacity can protect the hydrotalcite structure from decomposition in the NaCl solution. The reason for the improvement in the corrosion performance of Mg alloys can be attributed to the absorption and retention of the corrosive Cl^- ions, and the release of the inhibitive MoO_4^{2-} ions. In conclusion, the ion-exchange reaction of the HT-MoO_4^{2-} coating on the Mg alloy in chloride containing solution can be expressed as follows:

$$HT\text{-}MoO_4^{2-} + 2\ Cl^- \rightarrow HT\text{-}2Cl^- + MoO_4^{2-} \quad (3)$$

Based on the ion-exchange, the released MoO_4^{2-} ion concentrated on the coating surface led to the formation of a diffusion boundary layer, in which the concentrations of the MoO_4^{2-} ion are high enough to act as the anodic inhibitor to protect Mg alloys surface. By means of competitive adsorption, the presence of the MoO_4^{2-} in the diffusion boundary layer greatly impairs the adsorption of Cl^- on the surface of the coating. Therefore, the diffusion boundary layer with MoO_4^{2-} can effectively improve the pitting-resistance property on Mg alloys surface.

Simultaneously, the Mg corrosion reaction in diffusion boundary layer can be given as follows:

Anodic reaction:

$$Mg \rightarrow Mg^{2+} + 2e \quad (4)$$

Cathodic reaction:

$$2\ H_2O + 2e^- \rightarrow 2OH^- + H_2 \uparrow \quad (5)$$

The total reaction:

$$Mg + 2\ H_2O \rightarrow Mg(OH)_2 + H_2 \uparrow \quad (6)$$

The released MoO_4^{2-} ions can produce the following reactions[35]:

$$MoO_4^{2-} + 8\ H^+ + 3e^- \rightarrow Mo^{3+} + 4\ H_2O \quad (7)$$

At the same time, Mo^{3+} ions also consume the OH^- ions and create the formation of $Mo(OH)_3$. The $Mo(OH)_3$ compound is quite unstable and has a tendency which can transform into more stable compounds:

$$Mo^{3+} + 3OH^- \rightarrow Mo(OH)_3 \downarrow \quad (8)$$

$$Mo(OH)_3 + OH^- \rightarrow Mo(OH)_4 \downarrow \quad (9)$$

Also, based on the inhibiting mechanism of molybdate on steels[50-52], the MoO_4^{2-} ions may react with the dissolved Mg^{2+} to form a protective deposition film. The deposition of MoO_4^{2-} can inhibit the expansion and spreading of pitting corrosion. The probable reaction can be given as follows

$$Mg^{2+} + MoO_4^{2-} \rightarrow [MgMoO_4] \quad (10)$$

Journal of Materials Chemistry
Dynamic Article Links ▶
Cite this: DOI: 10.1039/c0xx00000x
www.rsc.org/xxxxxx

ARTICLE TYPE

Fig. 13

Fig. 13 Corrosion protection mechanism of the HT-MoO_4^{2-} coating

The above analysis implies that the ion-exchange ability of the layered structure and inhibiting activity of the molybdate ions make the coatings have the self-healing ability. The corrosion protection and inhibition mechanism of HT-MoO_4^{2-} coating can be divided in four parts: ion-exchange, competitive absorption, oxidation and deposition. On the basis of experimental results, the corrosion protection mechanism model of HT-MoO_4^{2-} coating is preliminarily proposed, and it is used to illustrate the mechanisms of ion-exchange, competitive adsorption, oxidation and deposition. In the model (Fig. 13), three layers from top to bottom are diffusion boundary layer, HT-MoO_4^{2-} coating and AZ31 substrate. From the modal, three clear conclusions should be obtained:

(1) Based on the ion-exchange, the released MoO_4^{2-} ions lead to the formation of a diffusion boundary layer.

(2) In the diffusion boundary layer, the released MoO_4^{2-} ions greatly impair the adsorption of Cl^- on the surface of the coating. Also, the released MoO_4^{2-} with the ability of oxidation and deposition can effectively reduce the damage of pitting corrosion to the substrate.

(3) In the HT-MoO_4^{2-} coating, the coexistence of HT-MoO_4^{2-} and HT-$2Cl^-$ can block the penetration of aggressive ions effectively, the corrosion pits can be healed by the $Mg(OH)_2$ layer and inhibiting MoO_4^{2-}.

5. Conclusions

(1) The molybdate intercalated hydrotalcite (HT-MoO_4^{2-}) coating with nano-sized lamellar structures was synthesized by the combination of the co-precipitation and the hydrothermal process on the AZ31 Mg alloy. The HT-MoO_4^{2-} coating consisted of compact, homogeneous and well-crystallized nanostructures can block the penetration of aggressive ions effectively.

(2) The LDH structure had the ion-exchange ability by absorbing and retaining aggressive Cl^- ions, and simultaneously releasing inhibiting MoO_4^{2-} ions. By means of competitive adsorption, protective deposition and oxidation reaction, the released MoO_4^{2-} ions acted as good anodic inhibitors to protect Mg alloys from attack.

(3) The HT-MoO_4^{2} coating as the nano-container of the inhibitor has a high stability and self-healing ability in the corrosive medium. The HT-MoO_4^{2-} coating has the potential to act as a smart coating capable of response to the stimuli from environment.

Acknowledgements

This work was supported by Scientific Research Foundation of Shandong for Outstanding Young Scientist (BS2013CL009), Doctoral Program Foundation of State Education Ministry (20133718120003), Applied Basic Research Foundation of Qingdao (13-1-4-217-jch) the open foundation of State Key Laboratory for Corrosion and Protection (SKLCP21012KF03) and Taishan Scholarship Project of Shandong Province (TS20110828).

References

1. G. Song, *Advanced Engineering Materials*, 2005, **7**, 563-586.
2. G. Song and A. Atrens, *Advanced Engineering Materials*, 2003, **5**, 837-858.
3. R. C. Zeng, J. Zhang, W. J. Huang, W. Dietzel, K. Kainer, C. Blawert and W. Ke, *Transactions of Nonferrous Metals Society of China*, 2006, **16**, s763-s771.
4. G. Makar and J. Kruger, *Journal of the Electrochemical Society*, 1990, **137**, 414-421.
5. J. Chen, Y. W. Song, D. Y. Shan and E. H. Han, *Transactions of Nonferrous Metals Society of China*, 2011, **21**, 936-942.
6. X. B. Chen, N. Birbilis and T. Abbott, *Corrosion Science*, 2012, **55**, 226-232.
7. N. Van Phuong, S. Moon, D. Chang and K. H. Lee, *Applied Surface Science*, 2012, **264**, 70-78.
8. W. Ke, E. H. Han, W. Q. Zhou and D. Y. Shan, Trans Tech Publ, 2003, pp. 879-882.
9. F. Chen, H. Zhou, B. Yao, Z. Qin and Q. Zhang, *Surface and Coatings Technology*, 2007, **201**, 4905-4908.
10. L. Xu and A. Yamamoto, *Colloids and Surfaces B: Biointerfaces*, 2012, **93**, 67-74.
11. W. J. Cheong, B. L. Luan and D. W. Shoesmith, *Corrosion science*, 2007, **49**, 1777-1798.
12. B. L. Yu and J. Y. Uan, *Scripta materialia*, 2006, **54**, 1253-1257.
13. J. Wöhle, C. Pfohl, K. T. Rie, A. Gebauer-Teichmann and S. Kim, *Surface and Coatings Technology*, 2000, **131**, 127-130.
14. M. Zheludkevich, *Self-healing materials: fundamentals, design strategies, and applications*, 2009, 101-140.
15. M. L. Zheludkevich, D. G. Shchukin, K. A. Yasakau, H. Möhwald and M. G. Ferreira, *Chemistry of Materials*, 2007, **19**, 402-411.
16. R. Ma, Z. Liu, L. Li, N. Iyi and T. Sasaki, *Journal of Materials Chemistry*, 2006, **16**, 3809-3813.
17. S. Guo, D. Li, W. Zhang, M. Pu, D. G. Evans and X. Duan, *Journal of Solid State Chemistry*, 2004, **177**, 4597-4604.
18. G. S. Kumar, E. Girija, A. Thamizhavel, Y. Yokogawa and S. N. Kalkura, *Journal of colloid and interface science*, 2010, **349**, 56-62.
19. R. Unnikrishnan and S. Narayanan, *Journal of Molecular Catalysis A: Chemical*, 1999, **144**, 173-179.
20. J. Wang, D. Li, X. Yu, X. Jing, M. Zhang and Z. Jiang, *Journal of Alloys and Compounds*, 2010, **494**, 271-274.
21. J. H. Syu, J. Y. Uan, M. C. Lin and Z. Y. Lin, *Corrosion Science*, 2012, **68**, 238-248.
22. F. Zhang, L. Zhao, H. Chen, S. Xu, D. G. Evans and X. Duan, *Angewandte Chemie International Edition*, 2008, **47**, 2466-2469.

23. J. Lin, C. Hsia and J. Uan, *Scripta materialia*, 2007, **56**, 927-930.
24. J. Lin and J. Uan, *Corrosion science*, 2009, **51**, 1181-1188.
25. J. K. Lin, K. L. Jeng and J. Y. Uan, *Corrosion Science*, 2011, **53**, 3832-3839.
26. J. K. Lin, J. Y. Uan, C. P. Wu and H. H. Huang, *Journal of Materials Chemistry*, 2011, **21**, 5011-5020.
27. J. Liu, Y. Li, X. Huang, G. Li and Z. Li, *Advanced Functional Materials*, 2008, **18**, 1448-1458.
28. J. Y. Uan, B. L. Yu and X. L. Pan, *Metallurgical and Materials Transactions A*, 2008, **39**, 3233-3245.
29. J. Chen, Y. Song, D. Shan and E. H. Han, *Corrosion Science*, 2012, **63**, 148-158.
30. J. Chen, Y. Song, D. Shan and E. H. Han, *Corrosion Science*, 2011, **53**, 3281-3288.
31. J. Chen, Y. Song, D. Shan and E. H. Han, *Corrosion Science*, 2012, **65**, 268-277.
32. J. Chen, Y. Song, D. Shan and E. H. Han, *Corrosion Science*, 2013, **74**, 130-138.
33. D. Li, F. Wang, X. Yu, J. Wang, Q. Liu, P. Yang, Y. He, Y. Wang and M. Zhang, *Progress in Organic Coatings*, 2011, **71**, 302-309.
34. Y. Lin, J. Wang, D. G. Evans and D. Li, *Journal of Physics and Chemistry of Solids*, 2006, **67**, 998-1001.
35. X. Yu, J. Wang, M. Zhang, L. Yang, J. Li, P. Yang and D. Cao, *Surface and Coatings Technology*, 2008, **203**, 250-255.
36. X. Yu, J. Wang, M. Zhang, P. Yang, L. Yang, D. Cao and J. Li, *Solid State Sciences*, 2009, **11**, 376-381.
37. E. Foad El-Sherbini, S. Abd-El-Wahab, M. Amin and M. Deyab, *Corrosion science*, 2006, **48**, 1885-1898.
38. J. Vega, N. Granizo, D. de la Fuente, J. Simancas and M. Morcillo, *Progress in Organic Coatings*, 2011, **70**, 213-219.
39. P. Chauhan, *Dessertation of Master of Technology*, 2010.
40. R. Zǎvoianu, R. Bîrjega, O. D. Pavel, A. Cruceanu and M. Alifanti, *Applied Catalysis A: General*, 2005, **286**, 211-220.
41. M. Jitianu, M. Bãlãsoiu, R. Marchidan, M. Zaharescu, D. Crisan and M. Craiu, *International Journal of Inorganic Materials*, 2000, **2**, 287-300.
42. M. A. Aramendía, V. Borau, C. Jiménez, J. M. Marinas, J. R. Ruiz and F. J. Urbano, *Journal of solid state chemistry*, 2002, **168**, 156-161.
43. S. Narayanan and K. Krishna, *Applied Catalysis A: General*, 1998, **174**, 221-229.
44. D. Carriazo, C. Martín and V. Rives, *Catalysis Today*, 2007, **126**, 153-161.
45. F. Millange, R. I. Walton and D. O'Hare, *Journal of Materials Chemistry*, 2000, **10**, 1713-1720.
46. A. Vreugdenhil, V. Gelling, M. Woods, J. Schmelz and B. Enderson, *Thin Solid Films*, 2008, **517**, 538-543.
47. M. Qian, A. Mcintosh Soutar, X. H. Tan, X. T. Zeng and S. L. Wijesinghe, *Thin Solid Films*, 2009, **517**, 5237-5242.
48. E. Ghali, W. Dietzel and K. U. Kainer, *Journal of Materials Engineering and Performance*, 2004, **13**, 7-23.
49. M. M. Avedesian and H. Baker, *ASM international*, 1999, **274**.
50. W. Robertson, *Journal of the electrochemical Society*, 1951, **98**, 94-100.
51. E. Lizlovs, *Corrosion*, 1976, **32**, 263-266.
52. J. Jefferies and B. Bucher, *Materials Performance;(United States)*, 1992, **31**.

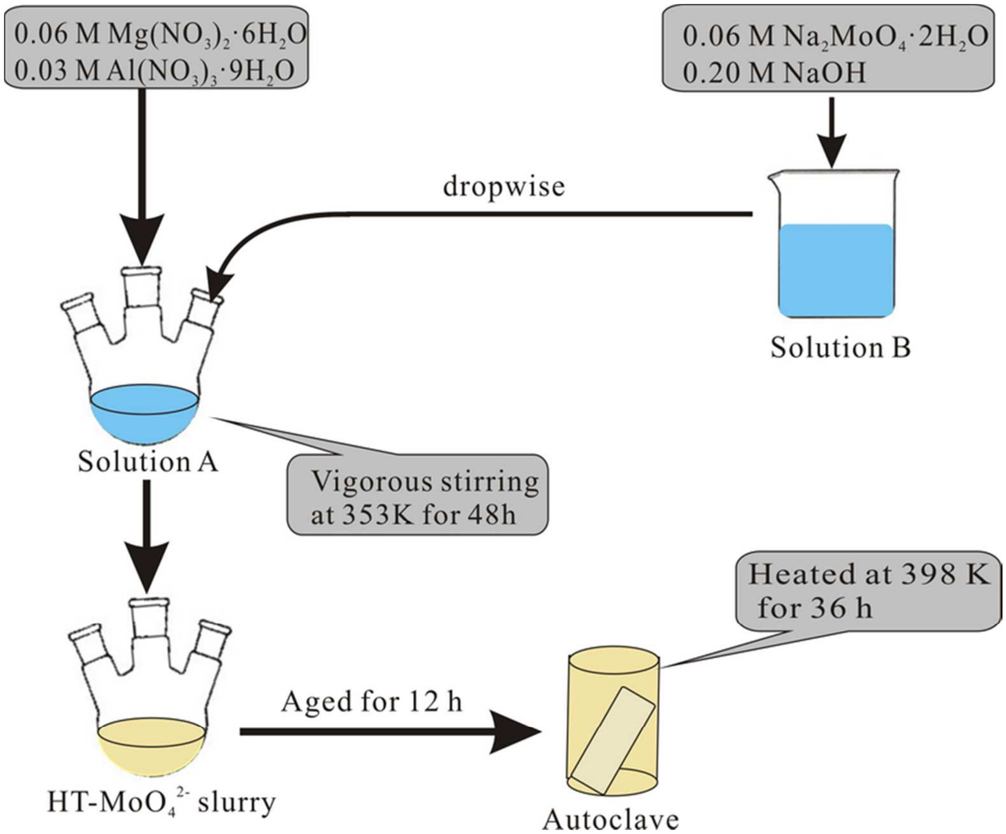

71x59mm (300 x 300 DPI)

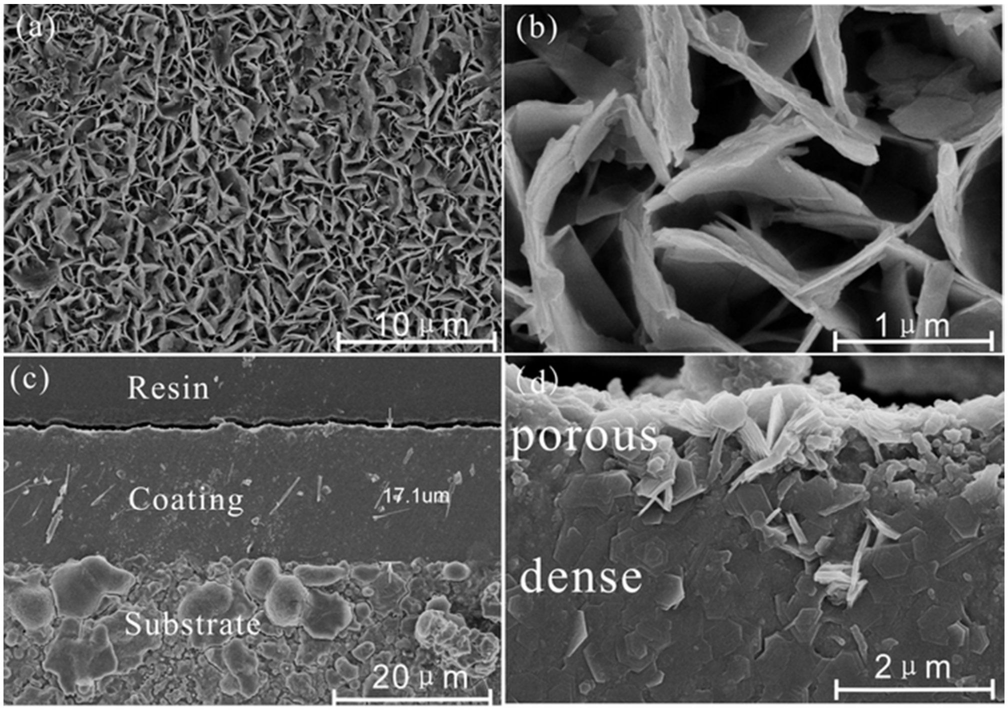

60x42mm (300 x 300 DPI)

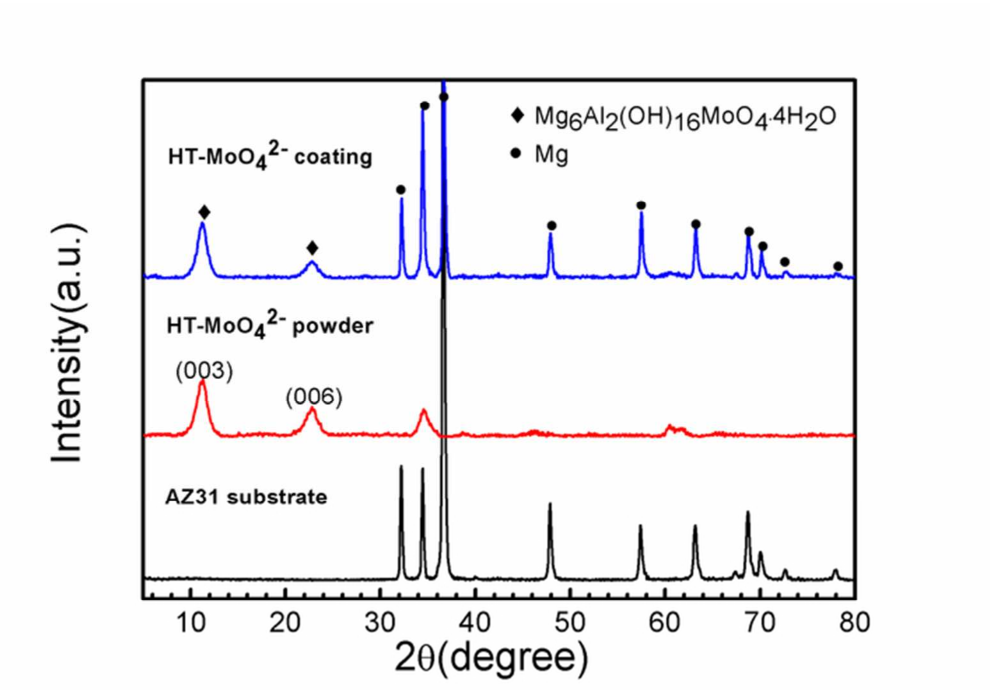

60x42mm (300 x 300 DPI)

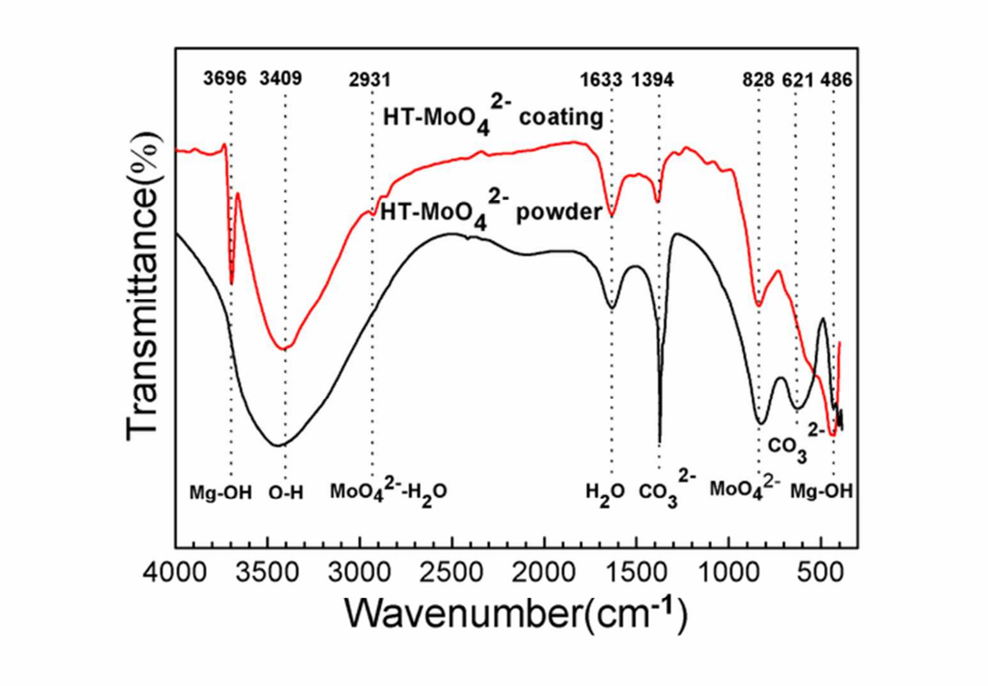

60x42mm (300 x 300 DPI)

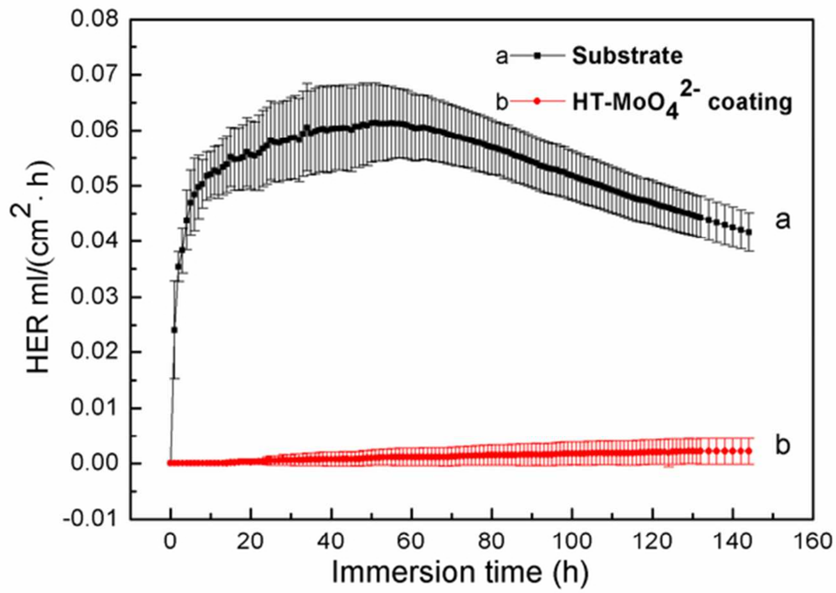

60x42mm (300 x 300 DPI)

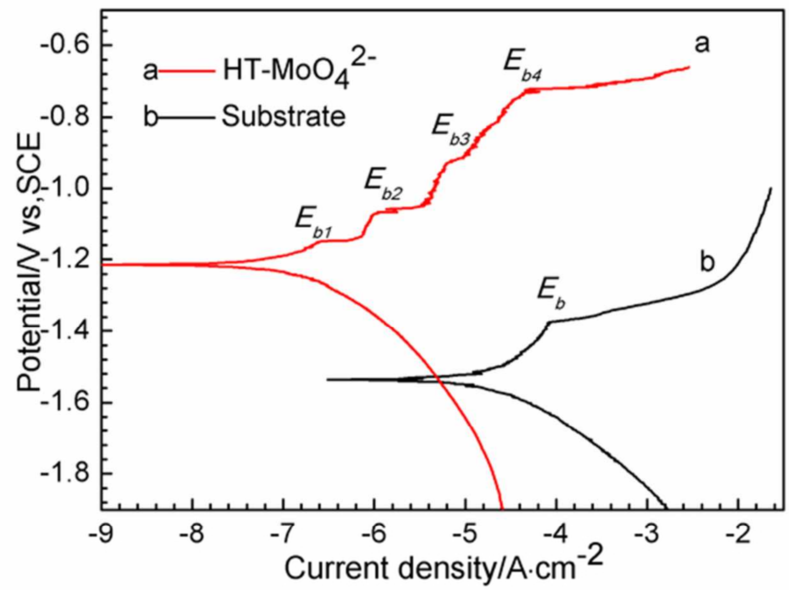

60x42mm (300 x 300 DPI)

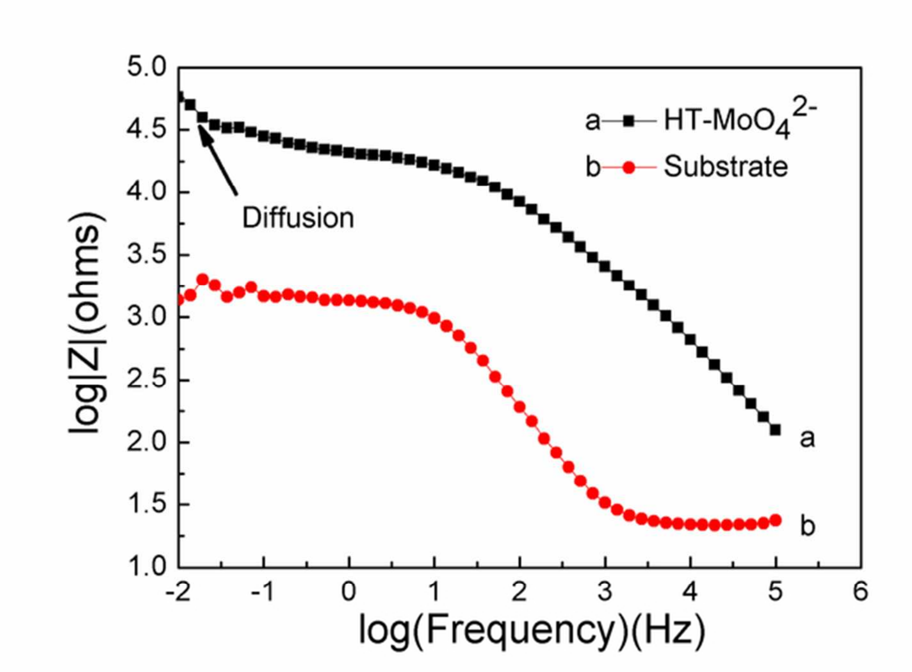

60x42mm (300 x 300 DPI)

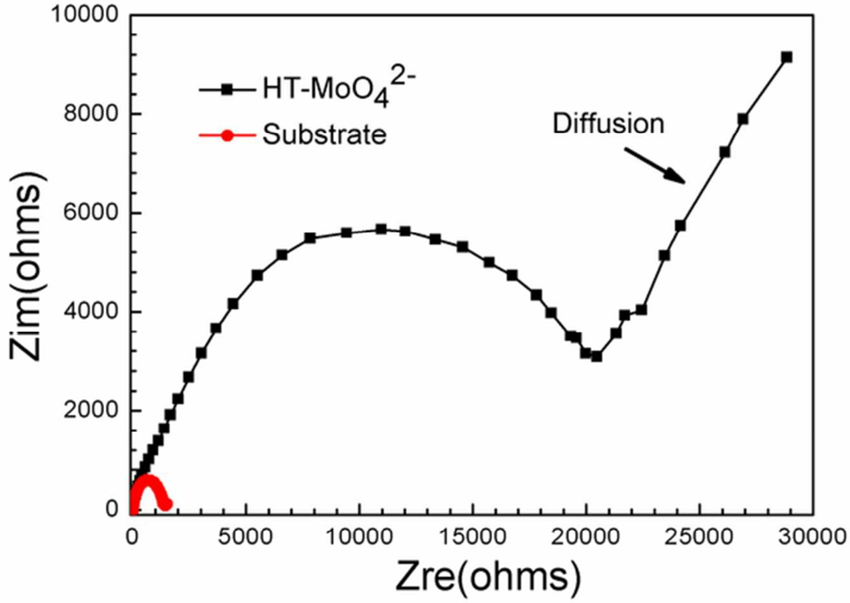

60x42mm (300 x 300 DPI)

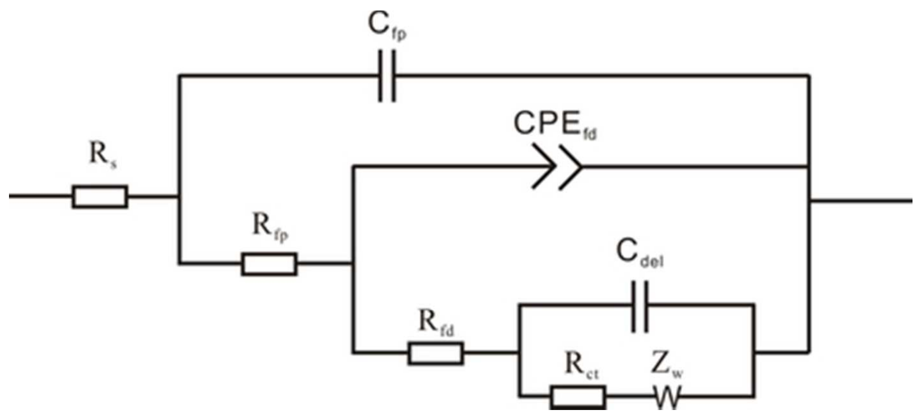

38x16mm (300 x 300 DPI)

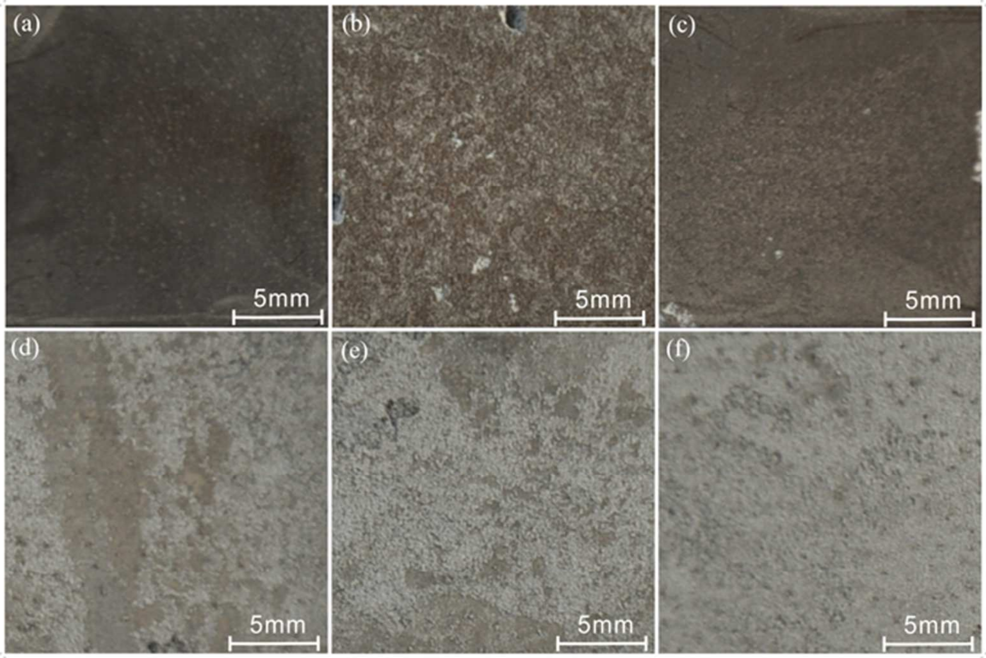

58x39mm (300 x 300 DPI)

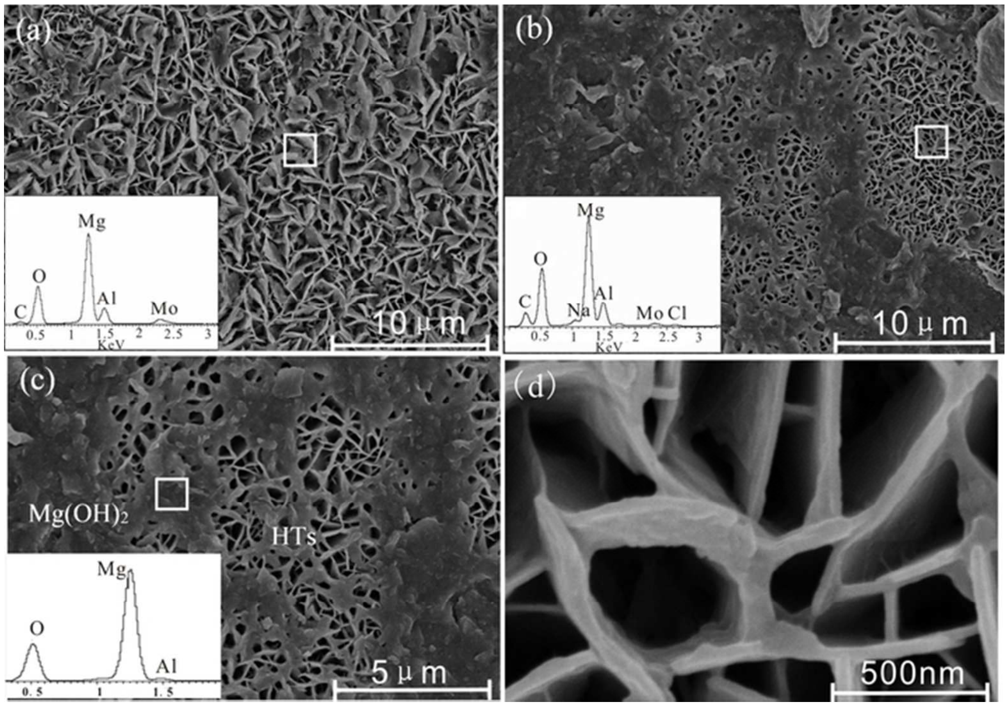

60x42mm (300 x 300 DPI)

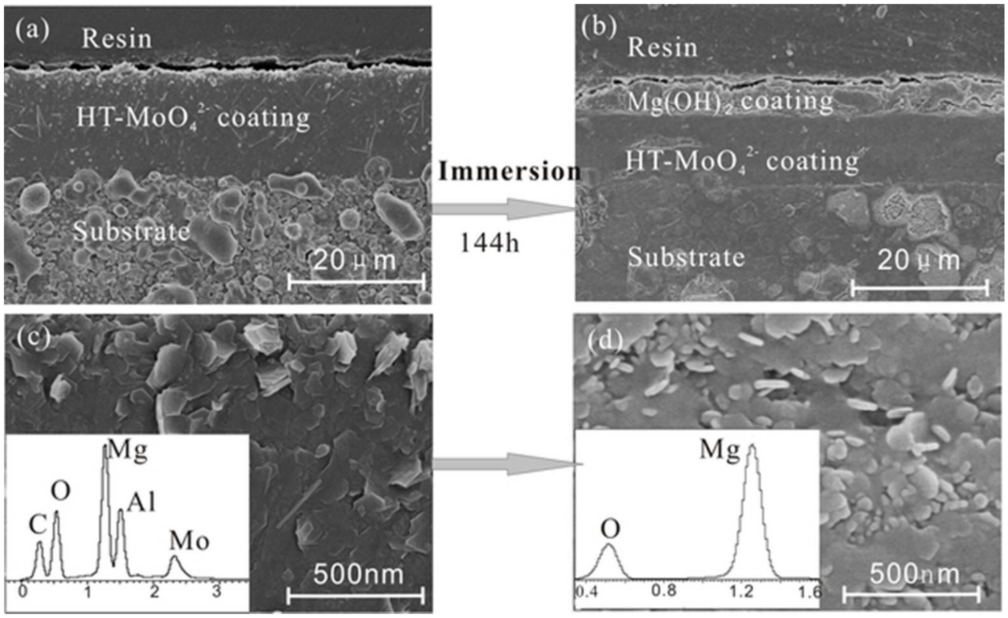

53x32mm (300 x 300 DPI)

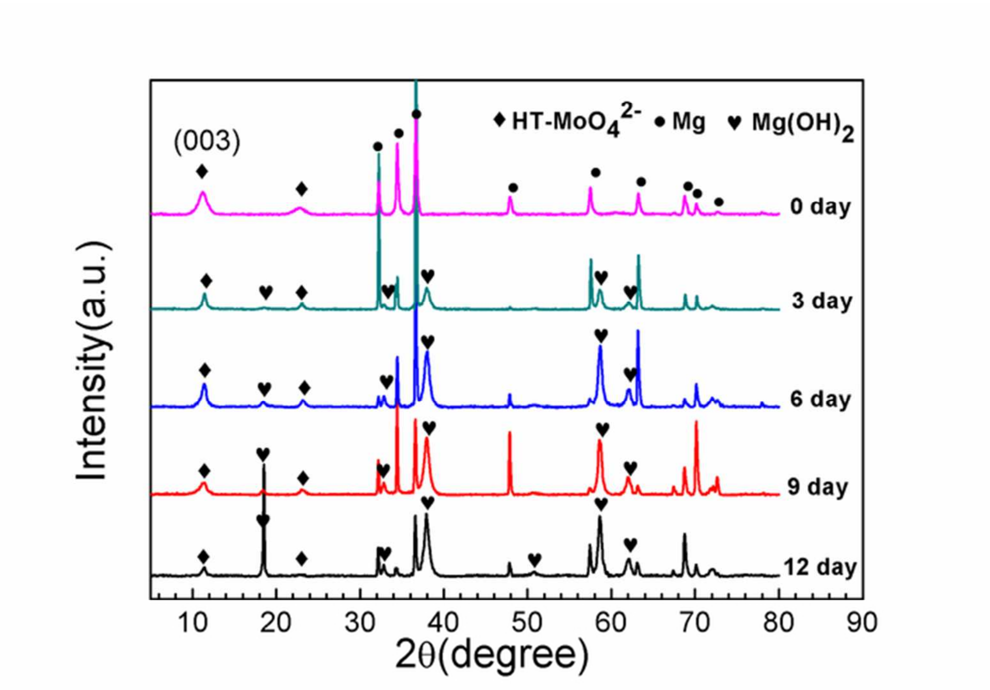

60x42mm (300 x 300 DPI)

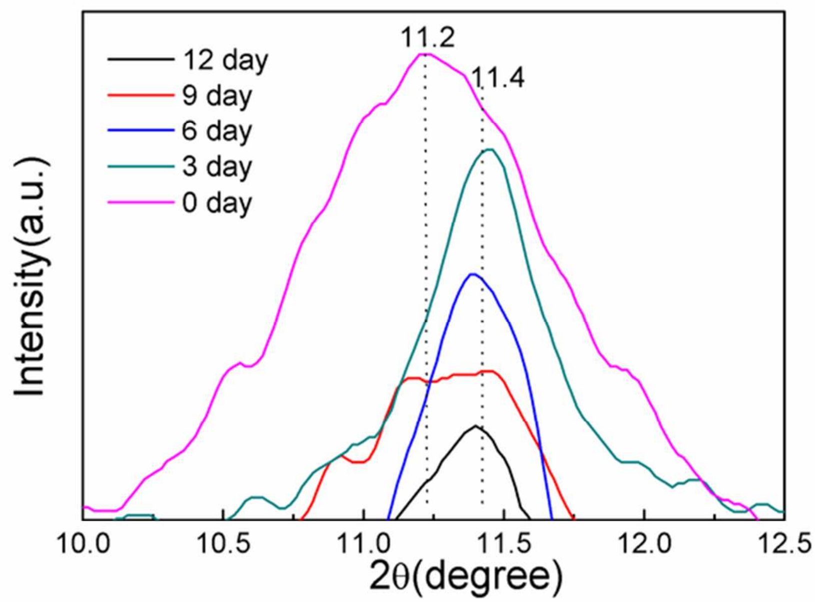

60x42mm (300 x 300 DPI)

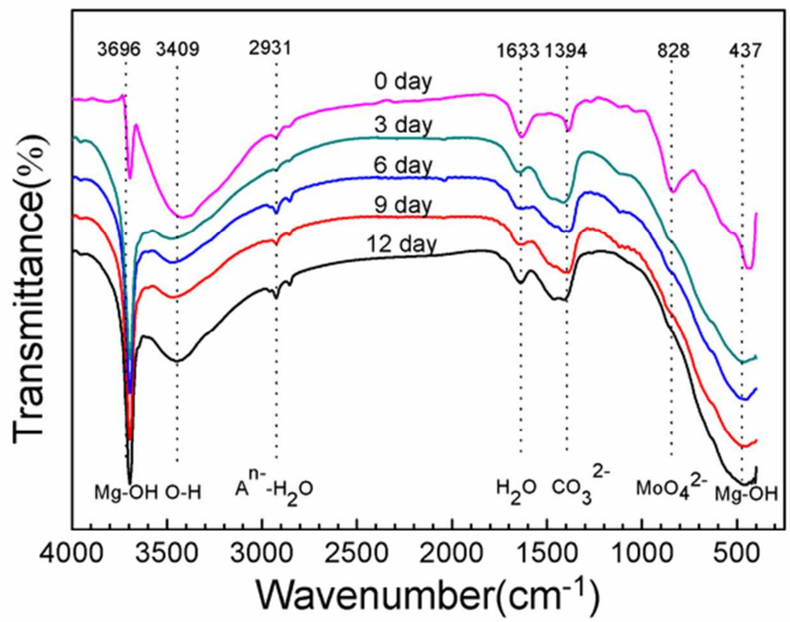

60x42mm (300 x 300 DPI)

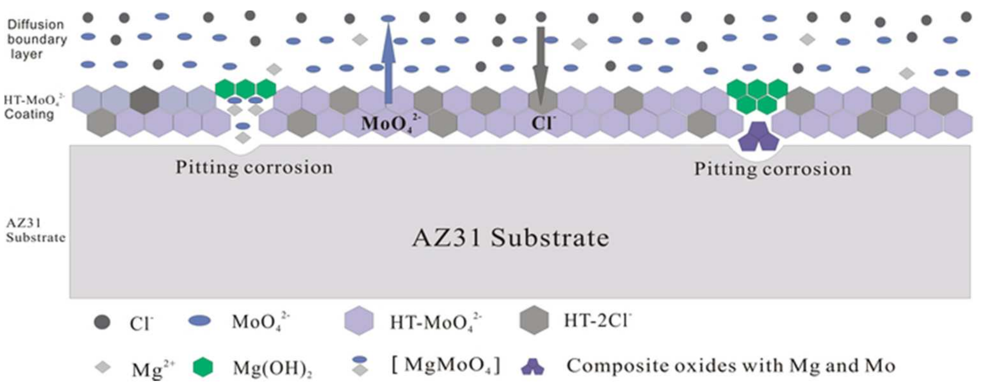

64x23mm (300 x 300 DPI)